Hydrogenation of Dimethyl Oxalate to Ethylene Glycol over Mesoporous Cu-MCM-41 Catalysts

Xinbin Ma, Hanwen Chi, Hairong Yue, Yujun Zhao, Yan Xu, Jing Lv, Shengping Wang, and Jinlong Gong
Key Laboratory for Green Chemical Technology of Ministry of Education, School of Chemical Engineering and Technology, Tianjin University, Tianjin 300072, China

DOI 10.1002/aic.13998
Published online January 11, 2013 in Wiley Online Library (wileyonlinelibrary.com)

The synthesis and utilization of mesoporous Cu-MCM-41 catalysts for hydrogenation of dimethyl oxalate to ethylene glycol is described in this article. Physicochemical properties of these Cu-MCM-41 catalysts have been investigated by N_2-physisorption, X-ray diffraction, inductively coupled plasma, N_2O titration, transmission electron microscopy, temperature programmed reduction, Fourier transform infrared spectroscopy, and X-ray photoelectron spectroscopy. It was found that the copper loading significantly influenced the pore structure and copper surface area of the catalyst. High catalytic performance is obtained over a 20Cu-MCM-41 catalyst with a full DMO conversion and EG yield of 92% at a LHSV of 3.0 h^{-1}. The catalytic performance of optimized 20Cu-MCM-41 catalyst could be attributed to the fine copper dispersion and large copper surface areas. © 2013 American Institute of Chemical Engineers *AIChE J*, 59: 2530–2539, 2013
Keywords: hydrogenation, ethylene glycol, syngas, copper particles

Introduction

Ethylene glycol (EG), a versatile chemical product with a huge market demand, is primarily used in polyester manufactures or to produce antifreeze. Synthesis of EG from syngas via oxidative coupling of CO to dimethyl oxalate (DMO) and further hydrogenation of DMO attracts increasing attention due to the shrinking of the fossil-fuel resource.[1,2] Because of homogeneous catalysts showing several disadvantages in the catalyst-products separation and the scaling up of the process, heterogeneous fix-bed catalysts were mostly used for the hydrogenation.[3] In the past decades, Cu–Cr bimetallic catalysts were widely investigated for the hydrogenation of DMO to EG.[4–6] However, the applications of the Cu–Cr catalysts were restricted because of the toxicity of chromium. Therefore, more recent work was focused on the development of supported copper-based catalysts for the DMO hydrogenation reactions. Carlini et al.[7] reported that strong acid sites of the support would catalyze the intermolecular dehydration of EG to ethanol, while strong basic sites promote the formation of 1,2-butanediol (1,2-BDO) via Guerbet reaction. Therefore, neutral support would be more preferred for the hydrogenation of DMO. To investigate the effect of the catalyst structures on the catalytic performance, Chen et al.[8] employed silica sol as a support to prepare Cu/SiO_2 catalysts and probed the effect of structure, composition, and copper dispersion on the catalytic performance. Yin et al.[9–12] systematically investigated the copper precursors, properties, structures, ion-exchange temperature, and the nature of active copper species of the copper-containing hexagonal mesoporous silica (HMS) catalysts, and the textural structure effect of mesoporous SiO_2 on the catalytic performance was found. Guo et al.[13] reported SBA-15 supported copper catalysts with a copper loading of 50 wt % for the hydrogenation of DMO. Our previous work explored Cu/SiO_2 monolithic catalysts for the reaction by using amorphous silica sol as a support, which showed the influence of composition and structure on catalytic performance.[14]

As M41S materials were successfully produced, many other types of mesoporous silica, e.g., HMS, SBA-15, and MCF,[15–17] were synthesized by using various organic template agents. As one of M41S family members, MCM-41 mesoporous molecular sieve has attracted considerable attention since its invention in 1992.[18] Owing to its exceptional adsorption capacities and molecular sieving properties such as high surface area, mesopore volume, suitable particle form, chemical and thermal stability and mechanical strength, MCM-41 is extensively applied in pharmaceutical, biological, and chemical industries, particularly for the separation processes and heterogeneous catalysis.[19–23] Moreover, MCM-41 can be easily synthesized by a hydrothermal synthesis method using cetyltrimethylammonium bromide (CTAB) as a structural direction agent at room-temperature. These features offer the metal ion incorporation possibility to modify the structure and catalytic properties of MCM-41 by substitution of Si atoms in regular tetrahedral positions. The incorporation of transition metals (e.g., Cu, Ti, Al, Ni, Zr, and Ag) into the MCM-41 framework uniformly with high contents and the corresponding meso-structural materials have been investigated by many researchers.[24–33] Compared to HMS, MCM-41 not only has the same hexagonal structure with large specific surface area, high pore volume, and adjustable pore size distribution, but also particularly has characteristics of extraordinarily regular structure and

Correspondence concerning this article should be addressed to J. Gong at jlgong@tju.edu.cn.

thinner wall of pores which is convenient for modification.[34] Different supports can influence the textural structure, particle size, and morphology of catalysts, further up the amount of catalytically active sites that contributes to the activity in the reaction. As far as we know, little attention has been paid on the application of MCM-41 for supporting base metal used in hydrogenation of oxalates. Especially, the structural effect of MCM-41 on the copper-based catalysts and thereof on the performance for DMO hydrogenation has not yet been reported.

In this work, copper-containing MCM-41 catalysts have been prepared by the ammonia-evaporation (AE) method with the aim of achieving a high catalytic performance of DMO hydrogenation. Catalysts with various copper loadings have been systematically characterized and tested for hydrogenation of DMO to EG. The influence of the copper loadings and the structural effect of MCM-41 have been examined in detail.

Experimental

Catalyst preparation

MCM-41. Mesoporous siliceous MCM-41 was prepared by the hydrothermal synthesis method using tetraethyoxysilane (TEOS) as a silica source and CTAB as a template agent. First, 11 g CTAB was dissolved in 270 g deionized water under vigorous stirring, and then 47 g TEOS was added to the surfactant solution followed by pH adjustment to ~11.0 through gradual addition of NaOH solution. The solution mixture was then stirred at 350 K for 2 h. The gels were loaded into a PTFE-lined stainless steel autoclave and heated at 373 K for 72 h. After cooling to room-temperature, the precipitated products were isolated by filtering, washed and dried in air at 373 K for 6 h. To remove the organic template materials, the dried samples were calcined in air at 823 K for 6 h with a heating rate of 1 K/min.

Cu-MCM-41. Cu-MCM-41 catalysts were prepared by the AE method described as follows: the required amount of $Cu(NO_3)_2{\cdot}3H_2O$ was dissolved in deionized water, and then ammonia aqueous solution was added and stirred for 0.5 h, followed by the MCM-41 powder addition and stirring for 4 h with the initial pH of the suspension adjusted to 11–12. The suspension was heated to 353 K to allow the evaporation of ammonia and the deposition of copper species on silica consequently. The residue was washed with deionized water followed by vacuum drying at 353 K for 10 h. The catalyst precursor was calcined at 673 K in air for 4 h. The catalysts were denoted as *x*Cu-MCM-41, where *x* represents copper mass concentrations (calculative 10–30 wt %).

Catalyst characterization

Textual properties of the samples were measured by a N_2 adsorption method using a Micromeritics Tristar II 3000 Analyzer instrument and a Micromeritics ASAP-2020 apparatus at 77 K. Mesoporous surface area was calculated from the desorption isotherms using the Brunauer–Emmet–Teller (BET) method and the pore-size distribution was determined by the Barrett–Joyner–Halenda (BJH) method from the desorption branches of the adsorption isotherms. Micropore properties were calculated from the isotherms using BET method and the pore-size distribution was determined by the Horvath–Kawazoe (HK) method from the desorption branches of the adsorption isotherms. The copper content in the final products was determined by an inductively coupled plasma optical emission spectrometry (ICP-OES) (Varian, Vista-MPX) operated at high frequency emission power of 1.5 kW and plasma airflow of 15.0 L/min. Sample was dissolved in the mixture of HNO_3, HF, and HBO_3, and then diluted with water. Fourier transform infrared (FT-IR) spectra of samples were recorded on a Nicolet 6700 spectrometer (Nicolet) using the standard KBr disk method. The effective region was from 400 to 4000 cm^{-1}.

H_2-TPR and N_2O titration were carried out on a Micromeritics Autochem II 2920. 50 mg catalyst was loaded into a quartz tube and dried in Ar atmosphere at 393 K for 1 h before the reduction. The catalyst was then heated in 5% H_2–Ar at flow rate of 30 ml/min with a heating rate of 10 K/min from room-temperature up to 1073 K. A thermal conductivity detector (TCD) was used to determine the amount of hydrogen consumption during this process. Specific surface areas of metallic copper were measured by the adsorption and decomposition of N_2O using the pulse titration method. Firstly, the sample was reduced at 623 K for 4 h under 5% H_2–Ar flow. After cooling to 363 K under pure He, 15% N_2O–He was pulsed in every 4 min with He as the carrier gas. And then the amount of hydrogen and N_2O consumption was determined by TCD. An adsorption stoichiometry of two Cu atoms per O atom and Cu surface density of 1.46×10^{19} Cu atoms per m^2 were assumed.

X-ray powder diffraction (XRD) was obtained on a Rigaku C/max-2500 diffractometer using Cu Kα radiation (λ = 1.5406 Å) at 40 eV and 100 mA. The small diffraction data of calcination samples were recorded at an interval of 0.01° and a scanning speed of 4°/min from $2\theta = 1°$ to $2\theta = 10°$. The wide-angle data were acquired by step scanning with a rate of 12°/min from $2\theta = 10°$ to $2\theta = 90°$. For the reduced samples, phase transformation may occur during exposure to an oxidative atmosphere. To avoid this process, catalysts were carefully collected under high purity N_2 at room-temperature and sealed in glass bottles prior to the XRD analysis. Copper crystallite size was calculated using the Scherrer equation.

Particle size and distribution were observed by transmission electron microscopy (TEM) using a Philips TECNAI G2 F20 system electron micro-scope at 100 kV. The reduced catalyst powder was dispersed in ethanol and applied onto a copper grid-supported transparent carbon foil and dried in air. X-ray photoelectron spectroscopy (XPS) analysis of the catalysts was carried out on a Perkin-Elmer PHI 1600 ESCA system operated at a pass energy of 187.85 eV for survey spectra with an Al KR X-ray source (E = 1486.6 eV).

Activity test

Hydrogenation of DMO to EG was performed on a continuous-flow stainless steel fixed-bed tubular reactor. The catalyst bed was packed with 0.4 g catalyst particles (40–60 meshes) tightly fitted to the wall of the stainless steel reactor. The catalyst bed had an inner diameter of 8 mm with a height of approximately 40 mm. The catalyst was activated in pure hydrogen atmosphere at 623 K for 4 h. After cooling to the reaction temperature of 474 K, the reactant (20 wt % DMO in methanol solution) was injected from the top of the reactor through a high-pressure pump (Lab Alliance Series II Pump). The reaction was carried out at a H_2/DMO molar ratio of 80 and a system pressure of 2.5 MPa. The liquid hourly space velocity (LHSV) of DMO was varied from 0.5

Table 1. Physical Properties of Synthesized *x*Cu-MCM-41 Catalysts

Catalyst	Cu loading[a] (%)	S_{BET}[b] (m^2/g)	S_{cu}[c] (m^2/g)	Cu[c] dispersion (%)	V_{pore}[b] (cm^3/g)	D_p[b] (nm)	D_{cu}[d] (nm)	D_{Cu}[e] (nm)
MCM-41	0	1008	–	–	0.81	2.5	–	–
10Cu-MCM-41	11.7	485	18.0	27.9	0.43	4.7	3.74	–
15Cu-MCM-41	15.6	368	22.5	23.3	0.45	4.7	4.48	–
20Cu-MCM-41	20.2	364	34.0	25.3	0.52	5.0	4.49	4.5
25Cu-MCM-41	24.7	161	29.7	18.5	0.24	5.7	5.65	5.3
30Cu-MCM-41	26.8	85	32.4	16.8	0.22	8.9	6.22	6.5

[a]Determined by ICP-AES analysis.
[b]Cu metal surface area determined by the N_2O titration method.
[c]Determined by BJH pore size distribution of N_2 adsorption in Figure 2.
[d]Copper particle size determined by the N_2O titration method.
[e]Calculated from the XRD data based on the Scherrer equation.

to 4.5 h^{-1}. The reaction products were condensed and analyzed on an Agilent Micro GC 6820 with an HP-innowax capillary column (Hewlett-Packard Company, 30 m × 0.32 mm × 0.50 μm) equipped with a flame ionization detector (FID). By-products included ethanol, methyl glycollate (MG), and 1,2-BDO. To ensure repeatability, four to eight separate GC samples were taken and the results were averaged for each experimental data point, and uncertainties were typically within 3%.

Results and Discussion

Textural properties of Cu-MCM-41

Textural properties of the mesoporous Cu-MCM-41 catalysts with different copper loadings are characterized and the results are listed in Table 1. The N_2 adsorption–desorption isotherms of calcined *x*Cu-MCM-41 samples are illustrated in Figure 1. Their pore-size distribution curves are shown in Figure 2.

As shown in Figure 1, all the copper-containing MCM-41 samples display a typical reversible Langmuir type IV isotherms with H1-type hysteresis loops,[35] which is a characteristic for a large-pore mesoporous material with 2-dimensional cylindrical channels. As well-known, MCM-41 has a hexagonal structure with regular parallel pores. The adsorption curve (Figure 1f) is very similar to the desorption curve, suggesting that the pore distribution is narrow and uniform. For *x*Cu-MCM-41 samples, the adsorption and desorption isotherm has an increasing step at a relative pressure of ~0.4–0.9 because of happening capillary condensation of N_2 inside the mesopore. It is suggested that the copper loading has great influence on the pore-size distribution. While for the copper-containing samples, the broad hysteresis loop in the isotherms indicates the wide distribution of mesopore existence.

As listed in Table 1, the as-synthesized MCM-41 had the BET specific surface area of 1008 m^2/g, large pore volume of 0.81 cm^3/g, and pore size at 2.5 nm. When the copper loadings increased from 11.7 to 26.8%, the BET specific surface areas decreased from 485 to 85 m^2/g; meanwhile, the average pore diameter rose from 4.7 to 8.9 nm. The average pore volume increased from 0.43 to 0.52 cm^3/g with the copper loading up to 20%, and then decreased to 0.22 cm^3/g with the copper loading continuing to increase. As shown in Figure 2, all the pores at ~2.5 nm disappeared, and a large number of secondary mesopores at ca. 5 nm appeared upon loading copper. These pores showed an increasing trend with the increment of copper loading. Moreover, the amount of micropore less than 1 nm decreased with increasing copper loading, proved by the pore-size distribution of mesoporous, as pore size at ~1.5 nm decreased as well. Therefore, we tentatively deduced that copper may incorporate into the walls of mesoporous silicate framework and block the pores to some extent when a small quantity of copper was introduced into MCM-41. The mesoporous framework was partially distorted and manifested irregular pore-size distribution. With the copper loading increased, agglomeration copper particles filled up the pore of ~2.5 nm and covered the surface of the support.

Copper dispersion of Cu-MCM-41 was characterized by the N_2O titration method. As listed in Table 1, the exposed copper surface area was firstly increscent and then decreasing. The largest copper surface area was obtained on 20Cu-MCM-41. The $[Cu(NH_3)_4]^{2+}$ entered into the pore channel of MCM-41, and grew up in the calcination process, which may collapse the silica walls. In addition, silica may transform to silicic acid when it was stirred in the alkaline solution, so the inerratic structural holes were partially destroyed. Because the copper grain sizes of calcined samples were bigger than the pore size of MCM-41, the original mesopores were blocked off and the secondary mesopores formed; therefore, the bigger pore size may be a benefit for the diffusion of

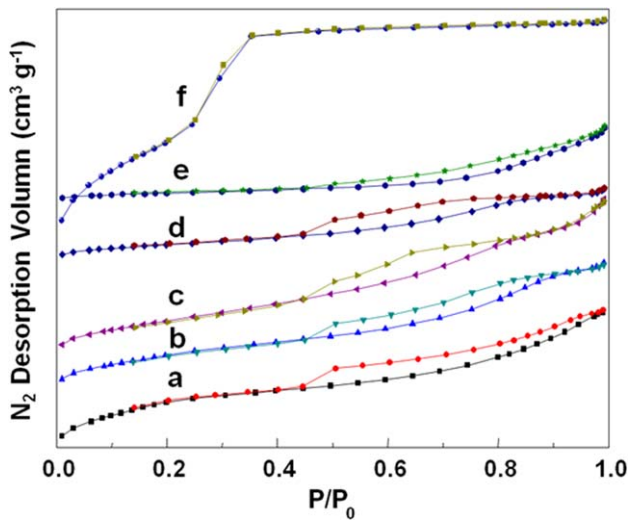

Figure 1. N_2 adsorption-desorption isotherms of the calcined catalysts with different copper loadings.

(a) 10Cu-MCM-41, (b) 15Cu-MCM-41, (c) 20Cu-MCM-41, (d) 25Cu-MCM-41, (e) 30Cu-MCM-41, and (f) MCM-41. [Color figure can be viewed in the online issue, which is available at wileyonlinelibrary.com.]

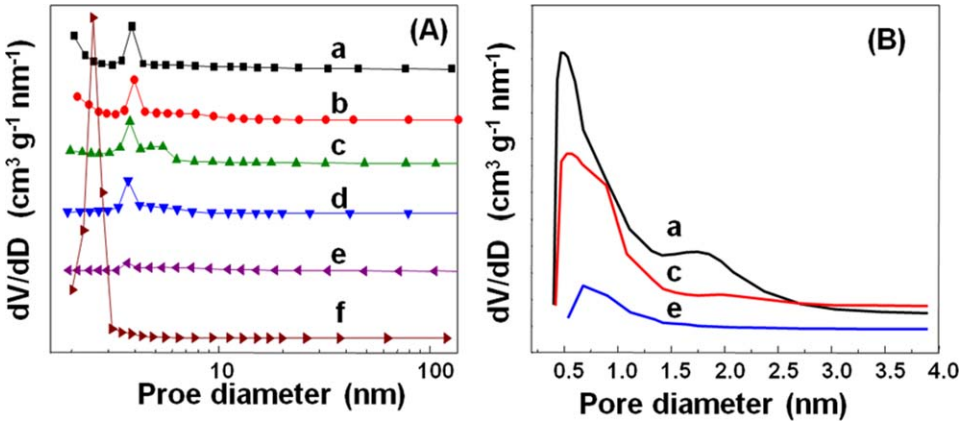

Figure 2. Mesoporous (A) and micropore (B) pore-size distribution of the calcined catalysts.

(a) 10Cu-MCM-41, (b) 15Cu-MCM-41, (c) 20Cu-MCM-41, (d) 25Cu-MCM-41, (e) 30Cu-MCM-41, and (f) MCM-41. [Color figure can be viewed in the online issue, which is available at wileyonlinelibrary.com.]

macromolecular DMO. 30Cu-MCM-41 exhibited a high surface copper, which was attributed to the relative higher copper loading, but the much smaller BET specific surface area limited the internal diffusion of the reactant and product.

Owing to a narrow and uniform pore-size distribution of MCM-41, copper particles grow up with the increase of copper loading. The walls of MCM-41 molecular sieve are generally thin, and not all metal heteroatoms can enter into the skeleton of MCM-41. Only part of the metal ion is exposed to the surface of MCM-41. Therefore, the interaction among the doped metal ions, the surface hydroxyl groups, and the wall of MCM-41 makes the pore sizes smaller. As copper particle size over all the Cu-MCM-41 catalysts is nearly twice of the pore size of MCM-41, the congestion gets serious until the micropores disappear mostly. (Figure 2).

FT-IR results

Figure 3 illustrates FT-IR spectra recorded for KBr-pelletized pure MCM-41, and unreduced *x*Cu-MCM-41 samples

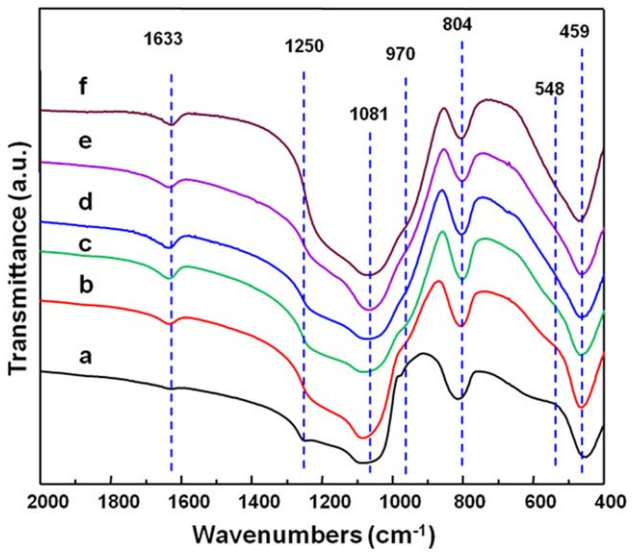

Figure 3. FT-IR spectra of different copper mass concentrations samples.

(a) MCM-41, (b) 10Cu-MCM-41, (c) 15Cu-MCM-41, (d) 20Cu-MCM-41, (e) 25Cu-MCM-41, and (f) 30Cu-MCM-41. [Color figure can be viewed in the online issue, which is available at wileyonlinelibrary.com.]

range from 400 to 2000 cm^{-1}. The asymmetric stretching vibrations of Si—O—Si bonds manifested an extension absorption band at 1081 cm^{-1} and a large shoulder at 1250 cm^{-1}. Similar phenomena were observed for Si—O—Si symmetric stretching at 804 cm^{-1} and bending mode at 459 cm^{-1}.[25] The band about 1633 cm^{-1} attributed to the characteristic band of OH groups of absorbed water on the catalyst surface. In addition, representative bands of the δ_{OH} in copper hydroxide are at 938 and 694 cm^{-1}, and the characteristic band for copper hydrosilicate is ~670 cm^{-1},[36] which were not found in FT-IR spectrum of the calcined *x*Cu-MCM-41 samples. The frequencies of the CuO bond characteristic for 575, 500, and 460 cm^{-1} were overlapped with the intensive adsorption band of Si—O—Si at 459 cm^{-1}, and just showed a shoulder peak at ~548 cm^{-1},[11,37] which was absent in MCM-41 curve and became more intensive as the copper loading increased.[38] Similar phenomena were observed for shoulder peak at 970 cm^{-1} assigned to the stretching vibrations of surface Si—O—Cu bond, which was overlapped with the broad intense absorption band at 1081 cm^{-1}. The intensity of the band at 970 cm^{-1} strengthened with the enrichment of copper in the framework of MCM-

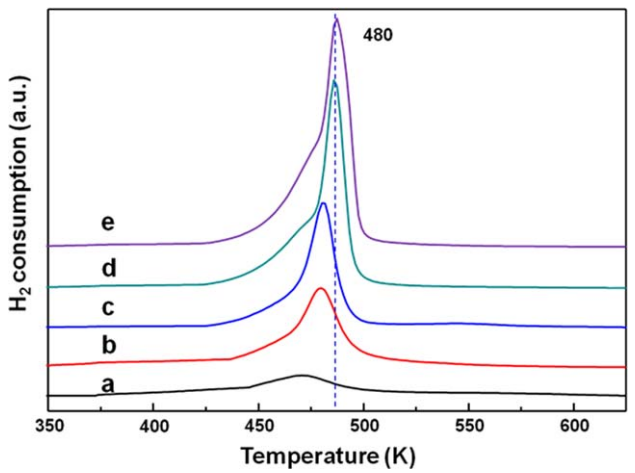

Figure 4. H_2-TPR profiles of the calcined samples.

(a) 10Cu-MCM-41, (b) 15Cu-MCM-41, (c) 20Cu-MCM-41, (d) 25Cu-MCM-41, and (e) 30Cu-MCM-41. [Color figure can be viewed in the online issue, which is available at wileyonlinelibrary.com.]

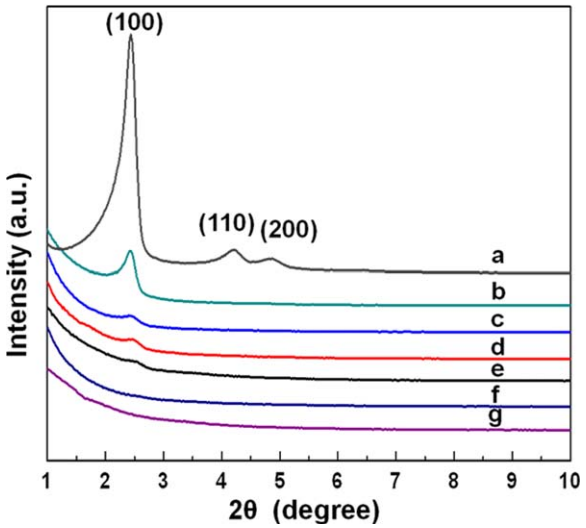

Figure 5. Low angle XRD patterns of the calcined catalysts with different copper loadings.

(a) MCM-41, (b) 5Cu-MCM-41, (c) 10Cu-MCM-41, (d) 15Cu-MCM-41, (e) 20Cu-MCM-41, (f) 25Cu-MCM-41, and (g) 30Cu-MCM-41. [Color figure can be viewed in the online issue, which is available at wileyonlinelibrary.com.]

41, resulting from the enhancement of the surface Si—O—Cu bond. The comparison of the shoulder peak at 970 cm^{-1} and the peak at 804 cm^{-1} could be a criterion of the copper incorporation into the framework of MCM-41. The increasing amount of Si—O—Cu band is along with the increment of copper loading. From the earlier results, we conclude that there is no copper hydroxide and copper hydrosilicate present in the calcined samples. The copper existence form is well dispersed CuO and Cu—O—Si, which is different from the structure of copper phyllosilicate prepared by using SiO_2 sol as a support.[8]

TPR results

The H_2-TPR profiles of samples with various copper loadings are shown in Figure 4. These spectra exhibited narrow and nearly symmetrical reduced peak centered at ca. 480 K, indicating a homogeneous dispersion and size of copper particles. The reduction peak shifting to high-temperature with increasing copper loading may be ascribed to increased copper particle sizes, poor dispersion, and strong interactions between copper oxide and support. The shoulder peak at ca. 468 K for the 30Cu-MCM-41 was found and vanished when copper loading was less than 25%, which may be attributed to the presence of the poor copper dispersion, weaker chemical bond of Cu—O—Si species with bigger particle sizes and partial big copper bulk. According to the reported Cu/SiO_2 and Cu-HMS,[9,11] the unique narrow reduction peak of the samples ($x < 25\%$) may be attributed to a single reduction step: $Cu^{2+} \rightarrow Cu^0$, indicating the well-dispersed copper species, while the absent peaks occurred at temperature higher than 523 K indicating the inexistence of copper crystal phase.[8] Marchi et al.[39] reported that the reduction of the Cu—O—Si species to Cu^+ on Cu/SiO_2 occurred at 523 K. Van Der Grift et al.[40] identified reduction peak at ~510 K due to the reduction of copper phyllosilicate to Cu^+ and of the well-dispersed CuO to Cu^0. Therefore, a two reduction step: $Cu^{2+} \rightarrow Cu^+ \rightarrow Cu^0$, possibly happened. However, due to the strong interaction between metal and support in Cu—O—Si species, the second process of the reduction requires a higher electrochemistry (0.52 V) than the first step (0.34 V), which would not occur under the present reduction condition.[9,39] Therefore, the only one strong reduction peak is attributed to the reduction of Cu—O—Si species overlapped by the reduction peak of the well-dispersed copper.

The above results imply a better copper dispersion in MCM-41 supported copper catalysts prepared by AE method. It is reported the reduction temperature of ion-exchanged Cu/SiO_2 samples at 523 K,[10,41] while silica sol, HMS, and SBA-15 supported copper catalysts at 516 K, ca. 517 K, and 543 K, respectively.[8,9,13]

XRD profiles

X-ray powder diffraction patterns of calcined and reduced *x*Cu-MCM-41 are shown in Figures 5 and 6. Small-angle diffraction patterns (Figure 5) show the characteristic structure of MCM-41. The strongest diffraction peak at $2\theta = 2.46°$ is

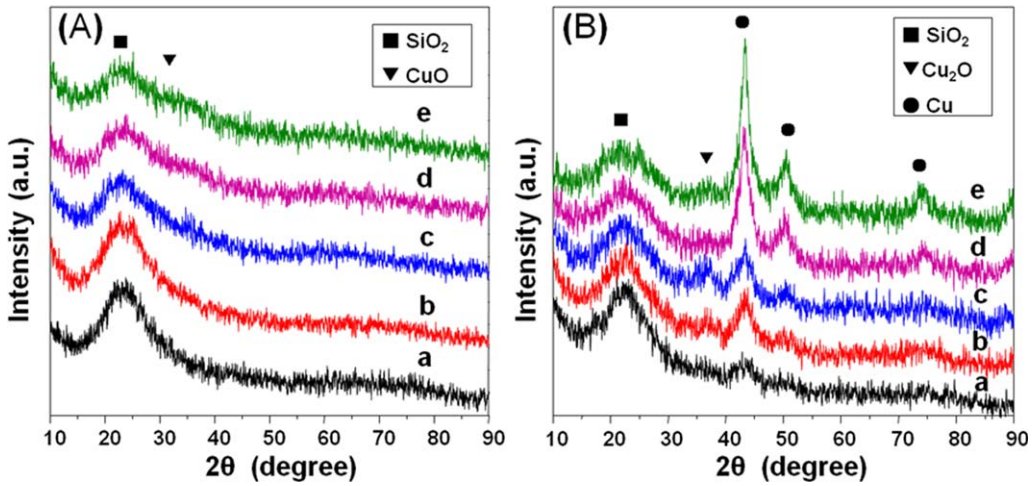

Figure 6. XRD patterns of the calcined (A) and reduced (B) catalysts with different copper loadings.

(a) 10Cu-MCM-41, (b) 15Cu-MCM-41, (c) 20Cu-MCM-41, (d) 25Cu-MCM-41, and (e) 30Cu-MCM-41. [Color figure can be viewed in the online issue, which is available at wileyonlinelibrary.com.]

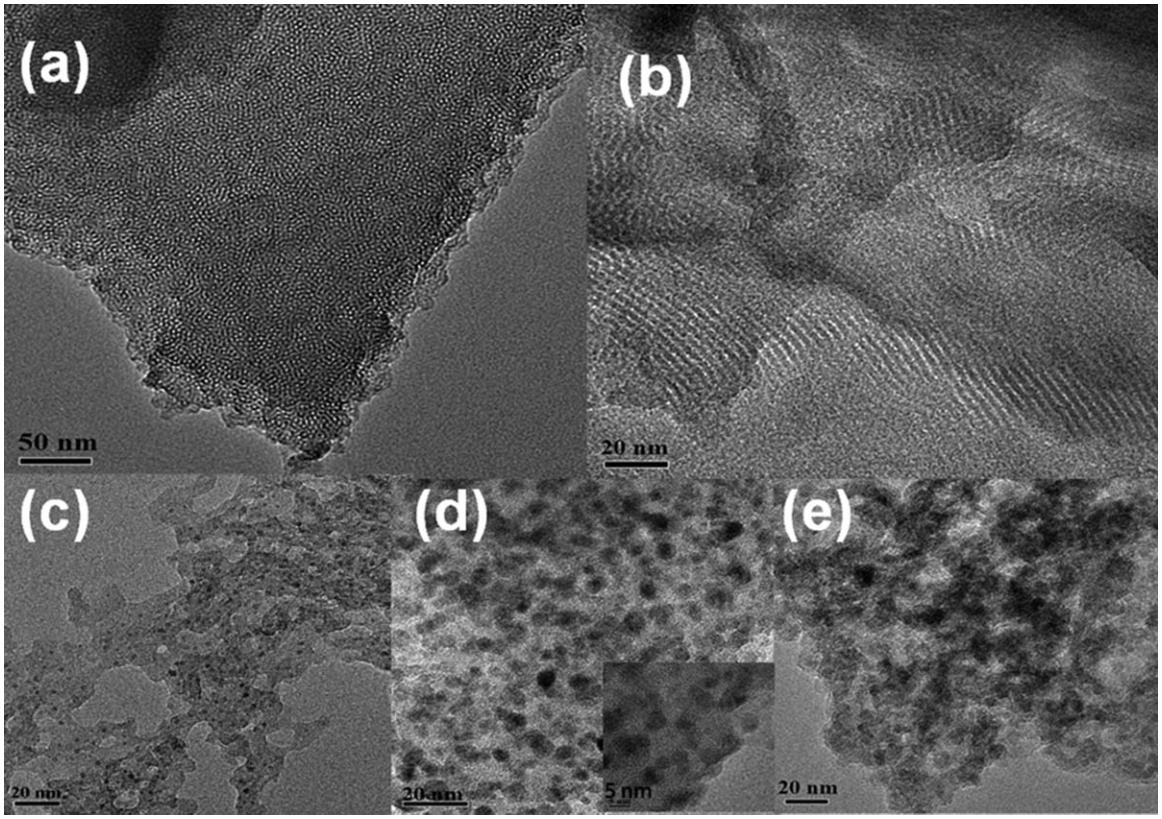

Figure 7. TEM images for MCM-41 and reduced *x*Cu-MCM-41 materials.

(a) and (b) MCM-41, (c) 10Cu-MCM-41, (d) 20Cu-MCM-41, and (e) 30Cu-MCM-41.

indexed with the (100) plane for a hexagonal unit cell and the other two weak peaks at $2\theta = 4.2°$ and $2\theta = 4.8°$ correspond to planes (110) and (200), respectively. Evidently, the samples show typical long-range order of hexagonal structure.[18] Both the diffraction peaks of (100) and (200) planes disappeared when copper was introduced into MCM-41. The intensity of (100) plane became weaker and nearly disappeared when copper loading reached 20%, presumably resulting from the collapse of the structure of MCM-41. This speculation is consistent with BET results. Although the characteristic structure of MCM-41 is almost destroyed, it could also provide big surface area and regular pore-size distribution for copper dispersion. Generally, the calcined Cu/SiO_2 samples exhibited characteristic peaks of CuO (tenorite) at 2θ of 35.4° and 38.6° (JCPDS05-0661). None of these peaks was found in the XRD patterns of *x*Cu-MCM-41 samples showed in Figure 6A, indicating that copper was highly dispersed in MCM-41. In addition, the feature at $2\theta = 22°$ was attributed to amorphous silica.

The XRD patterns of the reduced Cu-MCM-41 catalysts are shown in Figure 6B. The diffraction peak at 2θ of 43.3° along with two peaks at 51.1° and 74.1° can be assigned to

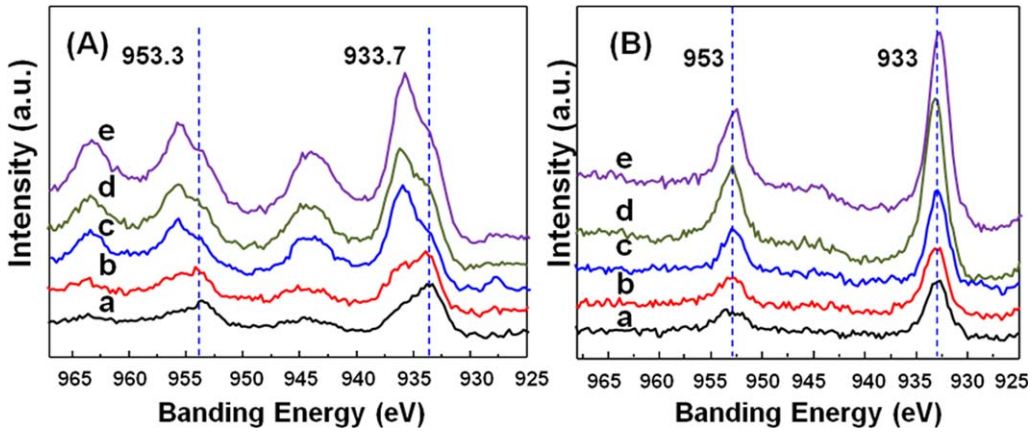

Figure 8. Cu 2p photoelectron spectra of the calcinated (A) and reduced (B) *x*Cu-MCM-41 samples.

(a) 10Cu-MCM-41, (b) 15Cu-MCM-41, (c) 20Cu-MCM-41, (d) 25Cu-MCM-41, (e) 30Cu-MCM-41. [Color figure can be viewed in the online issue, which is available at wileyonlinelibrary.com.]

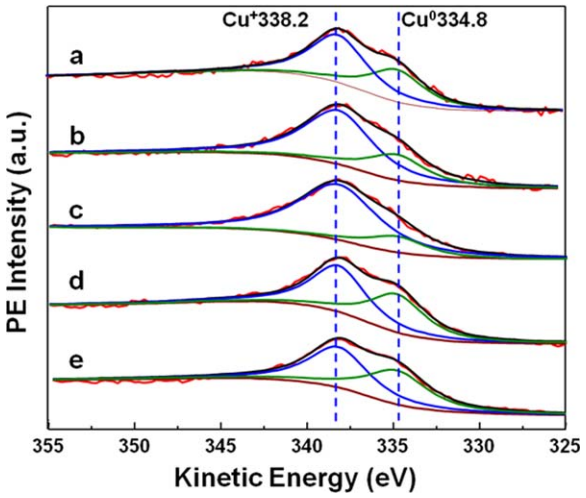

Figure 9. Cu LMM Auger spectra of the reduced *x*Cu-MCM-41 samples.

(a) 10Cu-MCM-41, (b) 15Cu-MCM-41, (c) 20Cu-MCM-41, (d) 25Cu-MCM-41, and (e) 30Cu-MCM-41. [Color figure can be viewed in the online issue, which is available at wileyonlinelibrary.com.]

metallic Cu species. As the copper loading increases, XRD peaks become more intensive and sharper. Therefore, the crystalline size of the copper particles, calculated based on the Scherrer equation (Table 1), showed an increasing trend with the increment of copper loading. All reduced catalysts showed a weak peak at around $2\theta = 36.8°$, which could be attributed to $Cu_2O(111)$ plane. Because of the strong interaction between the copper species and the silica, copper species reduction could be restricted and not be completely reduced to Cu^0, in accordance with FT-IR and TPR results.[11] The reduced 20Cu-MCM-41 catalysts exhibited the most distinct Cu_2O (111) diffraction peak, corresponding to Cu dispersion examined by N_2O titration listed in Table 1.

TEM results

TEM images of the as-synthesized MCM-41 and several reduced catalysts are shown in Figure 7. Specifically, MCM-41 shows a typical long-range order of hexagonal structure, dimensional homogeneity and ordered arrangement. As can be seen in Figures 7c and d, no bulk copper species condensed on the MCM-41 surface was found when the copper loading was below 20%. It is considered that the copper species were well dispersed in the MCM-41 mesoporous walls during the ammonia evaporation process. In Figure 7e, the deterioration of the copper dispersion could be observed clearly for 30Cu-MCM-41. The copper species size became bigger along with increasing copper loading in the reduction process, consistent with the XRD patterns of the reduced samples. When metal content in support arrived a certain degree, the structural superiority of MCM-41 was not affected. The restrain effect for reduction became weak, and copper particles were closely packed and could congregate easily.

Table 2. Cu Species on the Reduced *x*Cu-MCM-41 Catalyst Derived from Cu LMM XAES Spectra

Catalyst	X_{Cu^+} [a] (%)	X_{Cu^+} [b] (%)
10Cu-MCM-41	61.1	72.1
15Cu-MCM-41	71.2	76.7
20Cu-MCM-41	82.0	86.7
25Cu-MCM-41	54.4	62.3
30Cu-MCM-41	53.8	60.2

[a]Intensity ratio between Cu^+ and (Cu^+ + Cu^0) by deconvolution of Cu LMM XAES spectra.
[b]Calculated $Cu^+/(Cu^+ + Cu^0)$ determined by the N_2O titration method.

XPS

XPS measurements were carried out to evaluate surface composition and valence state of copper. As illustrated in Figure 8A, two intensive photoelectron peaks with the increase of copper loading at 933.7 eV and 953.3 eV were ascribed to the Cu $2p_{3/2}$ and $2p_{1/2}$ binding energy (BE), respectively, along with two satellite peaks at ~944 eV and ~963 eV. The shift of the peak from 933.7 eV to 936 eV was attributed to the electron afford–accept interaction of the copper and support (i.e., a better dispersion of copper oxide leading to a lower BE of Cu $2p_{3/2}$).[42] Upon reduction, showed in Figure 8B, these satellite signals attributed to an electron transfer from 2d ligand orbital to 3d core level vanished. The other peaks at ~933 eV and ~955 eV intensified, which were assigned to the doublet Cu $2p_{3/2}$ and Cu $2p_{1/2}$ levels for Cu^+ species. The satellite peak in Cu 2p spectra can be used to distinguish the Cu^{2+} and Cu^+ of Cu oxidation state. The main BE of Cu $2p_{3/2}$ at 933.7 eV became sharper and was shifted to 933 eV after reduction and the satellite peaks disappeared, which suggested that all the Cu^{2+} ions disappeared and translated to Cu^+ and Cu^0. Accordingly, we inferred that the Cu^+ species could be steadied on the surface and formed activity sites. One should note that the Cu^+ species is difficult to distinguish from Cu^0 by conventional XPS.

The ratio of band intensity in LMM XAES could be representative for the copper concentration on the catalyst surface and was used to distinguish the chemical states by their different kinetic energies in the line position.[43] The broad and asymmetric peak of the Cu LMM XAES spectra indicated that Cu^+ and Cu^0 may coexist in a stable state on the surface of Cu-MCM-41.[8–11,44] In general, 338.2 and 334.8 eV is ascribed to Cu^+ and Cu^0, respectively. The Cu LMM curves were deconvolute and the results are shown in Figure 9 and Table 2. The reduced catalysts showed different ratios of $Cu^+/(Cu^+ + Cu^0)$, due to the hindered reduction effect of the special structure of Cu-MCM-41. The ratio first rose and then decreased with the increment of copper loading, and the highest $Cu^+/(Cu^+ + Cu^0)$ was obtained on 20Cu-MCM-41, further confirmed by N_2O titration (Table 2).

Catalytic activities

Gas-phase hydrogenation of DMO reaction was carried out to investigate the catalytic performance of the Cu-MCM-41 catalysts with different copper loadings. It is known that the hydrogenation of DMO proceeds via MG to EG, while EG can be dehydrated further to ethanol (Scheme 1). The reaction between EG and ethanol on basic sites yields 1,2-BDO.[7,8] DMO conversion and EG and MG selectivity as

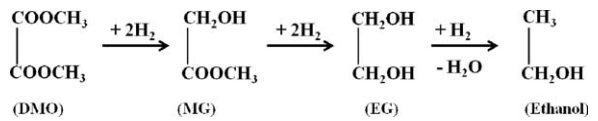

Scheme 1. Reaction scheme for the hydrogenation of DMO to MG, EG, and ethanol.

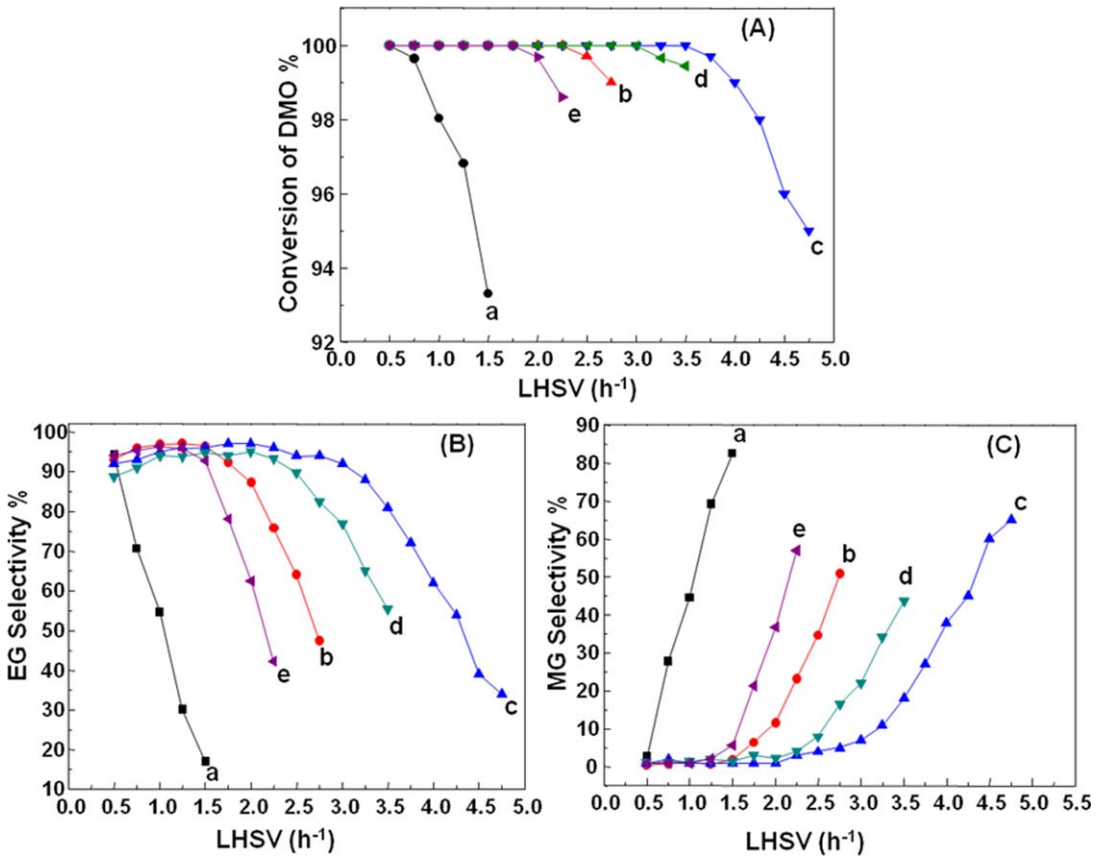

Figure 10. Effect of the LHSV of DMO conversion (A), EG (B) and MG (C) selectivity on the catalytic performance. Reaction conditions: P = 2.5 MPa, T = 473 K, H_2/DMO = 80.

(a) 10Cu-MCM-41, (b) 15Cu-MCM-41, (c) 20Cu-MCM-41, (d) 25Cu-MCM-41, and (e) 30Cu-MCM-41. [Color figure can be viewed in the online issue, which is available at wileyonlinelibrary.com.]

functions of LHSV are shown in Figure 10, respectively. Under a low LHSV of 0.5 h^{-1}, all of the catalysts showed high DMO conversion of 100% and high EG selectivity more than 90%. When the LHSV increases, the DMO conversion and EG selectivity decrease, while the MG selectivity increases. Under appropriate reaction conditions, the catalytic activity of Cu-MCM-41 increases steadily with the copper loading increasing from 10 to 20%, and then drops with the further increase from 20 to 30%. For instance, the DMO conversion of 20Cu-MCM-41 decreases when the LHSV exceeds 3.5 h^{-1}; meanwhile, the EG selectivity decreases and the MG selectivity increases obviously. The results may be attributed to the lack of catalytically active sites for conversion of DMO and hydrogenation of MG to EG at a higher LHSV. The optimal 20Cu-MCM-41 catalyst shows the best performance of 100% DMO conversion and 92% yield of EG at the LHSV of 3.0 h^{-1}.

We have shown that a higher copper dispersion and copper surface area could be obtained when the mesoporous MCM-41 is used as the support. The highest copper surface area (34 m^2/g) and the smaller copper particles with 4.5 nm could be obtained over the 20Cu-MCM-41 catalyst. For low copper-loading catalysts, the amount of active species is not enough for adsorption and conversion of DMO at a higher LHSV. The decrease in activity over the catalysts when the copper content exceed 20% could be attributed to the formation of less reducible aggregated copper particles. Due to the aggregation of a portion of CuO species during calcination, copper ions over the catalysts with higher copper loading may encapsulate in the mesoporous of MCM-41 and form large CuO particles, which decrease the surface active copper atoms and lead to a lower activity. In addition, the incorporation of copper into the walls of mesoporous silicate

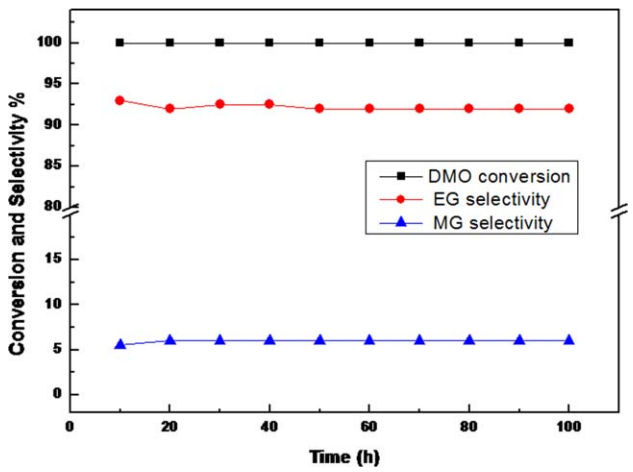

Figure 11. Stability of 20Cu-MCM-41 for hydrogenation of DMO.

Reaction conditions: P = 2.5 MPa, T = 473 K, H_2/DMO = 80, LHSV = 3.0 h^{-1}. [Color figure can be viewed in the online issue, which is available at wileyonlinelibrary.com.]

framework enhanced the interaction of metal with the support. The reduction of copper species could accordingly be restricted by the framework, leading to the coexistence of Cu^+ and Cu^0 on the surface. It is notable that the 20Cu-MCM-41 catalyst has a proper ratio of $Cu^+/(Cu^+ + Cu^0)$ and the largest Cu^+ surface area, accounting for the high activity.[45] Owing to the structural advantage of MCM-41, the catalyst with an optimal copper loading could finely disperse the copper and eliminate the mass-transfer limit of the reactants and products,[14] which results in an excellent stability as shown in Figure 11.

Conclusions

We have successfully prepared Cu-MCM-41 catalysts through the ammonia-evaporation method and found that copper may incorporate into the walls of mesoporous silicate framework and block the pores to some extent when a small quantity of copper was introduced into MCM-41. Catalysts with appropriate copper loading show high copper dispersion and copper surface area, small particle size, and high sintering resistance. Moreover, excellent catalytic performance for hydrogenation of DMO to EG could be obtained on the Cu-MCM-41 catalysts with an optimized copper loading of about 20%, achieving 100% conversion of DMO and more than 95% selectivity to EG.

Acknowledgments

We are grateful for the financial support from the National Science Foundation of China (21276186, 21222604), National High Technology Research and Development Program of China (2011AA051002), the Program for New Century Excellent Talents in University (NCET-10-0611), China Postdoctoral Science Foundation (20090450090), Seed Foundation of Tianjin University (60303002), and the Program of Introducing Talents of Discipline to Universities (B06006).

Literature Cited

1. Xu G, Li Y, Li Z, Wang H. Kinetics of the hydrogenation of diethyl oxalate to ethylene glycol. *Ind Eng Chem Res*. 1995;34(7):2371–2378.
2. Yue H, Zhao Y, Ma X, Gong J. Ethylene glycol: properties, synthesis, and applications. *Chem Soc Rev*. 2012;41(11):4218–4244.
3. Van Engelen MC, Teunissen HT, De Vries JG, Elsevier CJ. Suitable ligands for homogeneous ruthenium-catalyzed hydrogenolysis of esters. *J Mol Catal A: Chemical*. 2003;206(1–2):185–192.
4. Zehner LR, Lenton RW, Inventors. US patent 4,112,245. 1978.
5. Haruhiko M, Kouichi H, Taizou U, Yasuo N, Seizou I, Takanori T. Inventors. US patent 57,123,127. 1982.
6. Susumu T, Kozo F, Keigo N, Masaoki M, Katsuhiko M. Inventors. US patent 0,046,983. 1982.
7. Carlini C, Di Girolamo M, Macinai A, Marchionna M, Noviello M, Galletti A, Sbrana G. Selective synthesis of isobutanol by means of the Guerbet reaction: Part 2. Reaction of methanol/ethanol and methanol/ethanol/n-propanol mixtures over copper based/MeONa catalytic systems. *J Mol Catal A: Chemical*. 2003;200(1–2):137–146.
8. Chen L, Guo P, Qiao M, Yan S, Li H, Shen W, Xu H, Fan K. Cu/SiO_2 catalysts prepared by the ammonia-evaporation method: texture, structure, and catalytic performance in hydrogenation of dimethyl oxalate to ethylene glycol. *J Catal*. 2008;257(1):172–180.
9. Yin A, Guo X, Dai W, Li H, Fan K. Highly active and selective copper-containing HMS catalyst in the hydrogenation of dimethyl oxalate to ethylene glycol. *Appl Catal A: General*. 2008;349(1–2):91–99.
10. Yin A, Guo X, Fan K, Dai W. Influence of copper precursors on the structure evolution and catalytic performance of Cu/HMS catalysts in the hydrogenation of dimethyl oxalate to ethylene glycol. *Appl Catal A: General*. 2010;377(1–2):128–133.
11. Yin A, Guo X, Dai W, Fan K. The nature of active copper species in Cu-HMS Catalyst for hydrogenation of dimethyl oxalate to ethylene glycol: new Insights on the synergetic effect between Cu^0 and Cu^+. *The Journal of Physical Chemistry C*. 2009;113(25):11003–11013.
12. Yin A, Guo X, Fan K, Dai W. Ion-exchange temperature effect on Cu/HMS Catalysts for the hydrogenation of dimethyl oxalate to ethylene glycol. *ChemCatChem*. 2010;2(2):206–213.
13. Guo X, Yin A, Dai W, Fan K. One pot synthesis of ultra-high copper contented Cu/SBA-15 Material as excellent catalyst in the hydrogenation of dimethyl oxalate to ethylene glycol. *Catal Lett*. 2009;132(1–2):22–27.
14. Yue H, Zhao Y, Zhao L, Lv J, Wang S, Gong J, Ma X. Hydrogenation of dimethyl oxalate to ethylene glycol on a Cu/SiO_2/cordierite monolithic catalyst: enhanced internal mass transfer and stability. *AIChE J*. 2012(9):2798–2809.
15. Tanev PT, Pinnavaia TJ. A neutral templating route to mesoporous molecular sieves. *Science*. 1995;267(5199):865–867.
16. Schmidt Winkel P, Lukens WW, Zhao D, Yang P, Chmelka BF, Stucky GD. mesocellular siliceous foams with uniformly sized cells and windows. *Journal of the American Chemical Society*. 1998;121(1):254–255.
17. Zhao D, Feng J, Huo Q, Melosh N, Fredrickson G, Chmelka B, Stucky G. Triblock copolymer syntheses of mesoporous silica with periodic 50 to 300 angstrom pores. *Science*. 1998;279(5350):548–552.
18. Beck J, Vartuli J, Roth W, Leonowicz M, Kresge C, Schmitt K, Chu C, Olson D, Sheppard E. A new family of mesoporous molecular sieves prepared with liquid crystal templates. *J Am Chem Soc*. 1992;114(27):10834–10843.
19. Qian KK, Bogner RH. Application of mesoporous silicon dioxide and silicate in oral amorphous drug delivery systems. *J Pharm Sci*. 2012;101(2):444–463.
20. Lin C, Cheng H. Application of mesoporous catalysts over palm-oil biodiesel for adjusting fuel properties. *Energy Convers Manage*. 2012;53(1):128–134.
21. Chen X, Lam KF, Yeung KL. Selective removal of chromium from different aqueous systems using magnetic MCM-41 nanosorbents. *Chem Eng J*. 2011;172(2–3):728–734.
22. Kawi S, Lai MW. Supercritical fluid extraction of surfactant from Si-MCM-41. *AIChE J*. 2002;48(7):1572-1580.
23. Tan Q, Fan Y, Liu H, Song T, Shi G, Shen B, Bao X. Bimodal micro-mesoporous aluminosilicates for heavy oil cracking: Porosity tuning and catalytic properties. *AIChE J*. 2008;54(7):1850–1859.
24. Chen LY, Jaenicke S, Chuah GK. Thermal and hydrothermal stability of framework-substituted MCM-41 mesoporous materials. *Microporous Mater*. 1997;12(4–6):323–330.
25. Shi Y, Wang S, Ma X. Microwave preparation of Ti-containing mesoporous materials. Application as catalysts for transesterification. *Chem Eng J*. 2011;166(2):744–750.
26. Xia M, Long M, Yang Y, Chen C, Cai W, Zhou B. A highly active bimetallic oxides catalyst supported on Al-containing MCM-41 for Fenton oxidation of phenol solution. *App Catal B: Environmental*. 2011;110:118–125.
27. Castro K, Paulino A, Silva E, Chellappa T, Lago M, Fernandes V, Araujo A. Effect of the AL-MCM-41 catalyst on the catalytic pyrolysis of atmospheric petroleum residue (ATR). *J Therm Anal Calorim*. 2011;106(3):759–762.
28. Wu C, Wang L, Williams PT, Shi J, Huang J. Hydrogen production from biomass gasification with Ni/MCM-41 catalysts: influence of Ni content. *Appl Catal B: Environmental*. 2011;108–109:6–13.
29. Yin A, Wen C, Dai W, Fan K. Ag/MCM-41 as a highly efficient mesostructured catalyst for the chemoselective synthesis of methyl glycolate and ethylene glycol. *Appl Catal B: Environmental*. 2011;108–109:90–99.
30. Bachari K, Chebout R, Guerroudj RM, Lamouchi M. Preparation and characterization of Zr-MCM-41 synthesized under microwave irradiation condition for acetylation of 1,2-dimethoxybenzene with acetic anhydride. *Res Chem Intermed*. 2011;38(2):367–381.
31. Rath D, Parida KM. Copper and nickel modified MCM-41 an efficient catalyst for hydrodehalogenation of chlorobenzene at room temperature. *Ind Eng Chem Res*. 2011;50(5):2839–2849.
32. Jana S, Bhunia S, Dutta B, Koner S. Anchoring of copper(II) complexes onto the organically modified MCM-41: preparation, characterization and catalytic epoxidation. *Appl Catal A: General*. 2011;392(1–2):225–232.

33. Wang P, Zheng X, Wu X, Wei X, Zhou L. Preparation and characterization of CuO nanoparticles encapsulated in mesoporous Silica. *Microporous Mesoporous Mater*. 2012;149(1):181–185.
34. Tanev PT. A Neutral Templating Route to Mesoporous Molecular Sieves and their Catalytic Application for Peroxide Oxidation of Large Aromatic Molecules, Dept. of Chemistry, Michigan State University; 1995.
35. Schmidt R, Hansen EW, Stoecker M, Akporiaye D, Ellestad OH. Pore size determination of MCM-51 mesoporous materials by means of 1H NMR spectroscopy, N2 adsorption, and HREM. A preliminary study. *J Am Chem Soc*. 1995;117(14):4049–4056.
36. Toupance T, Kermarec M, Lambert JF, Louis C. Conditions of formation of copper phyllosilicates in silica-supported copper catalysts prepared by selective adsorption. *J Phys Chem B*. 2002;106(9):2277–2286.
37. Diaz G, Perez Hernandez R, Gomez Cortes A, Benaissa M, Mariscal R, Fierro J. CuO-SiO2 sol-gel catalysts: characterization and catalytic properties for NO reduction. *J Catal*. 1999;187(1):1–14.
38. Cordoba G, Arroyo R, Fierro J, Viniegra M. Study of xerogel-glass transition of CuO/SiO2. *J Solid State Chem*. 1996;123(1):93–99.
39. Marchi AJ, Fierro JLG, Santamaría J, Monzón A. Dehydrogenation of isopropylic alcohol on a Cu/SiO2 catalyst: a study of the activity evolution and reactivation of the catalyst. *Appl Catal A: General*. 1996;142(2):375–386.
40. Van Der Grift C, Wielers A, Jogh B, Van Beunum J, De Boer M, Versluijs-Helder M, Geus J. Effect of the reduction treatment on the structure and reactivity of silica-supported copper particles. *J Catal*. 1991;131(1):178–189.
41. Chary KVR, Seela KK, Sagar GV, Sreedhar B. Characterization and reactivity of niobia supported copper oxide catalysts. *J Phys Chem B*. 2003;108(2):658–663.
42. Chary KVR, Sagar GV, Srikanth CS, Rao VV. Characterization and catalytic functionalities of copper oxide catalysts supported on zirconia. *J Phys Chem B*. 2006;111(3):543–550.
43. Liu Z, Amiridis MD, Chen Y. Characterization of CuO supported on tetragonal ZrO_2 catalysts for N_2O decomposition to N_2. *J Phys Chem B*. 2005;109(3):1251–1255.
44. Dai W, Sun Q, Deng J, Wu D, Sun Y. XPS studies of Cu/ZnO/Al_2O_3 ultra-fine catalysts derived by a novel gel oxalate co-precipitation for methanol synthesis by CO_2+H_2. *Appl Sur Sci*. 2001;177(3):172–179.
45. Gong J, Yue H, Zhao Y, Zhao S, Zhao L, Lv J, Wang S, Ma X. Synthesis of ethanol via syngas on Cu/SiO_2 catalysts with balanced Cu^0-Cu^+ sites. *J Am Chem Soc*. 2012;34(134):13922–13925.

Manuscript received Apr. 10, 2012, and revision received Nov. 26, 2012.